Journal of Materials Chemistry A

ROYAL SOCIETY OF CHEMISTRY

PAPER

View Article Online
View Journal

Cite this: DOI: 10.1039/d6ta00082g

Reimagining interface processing in solid-state batteries *via* electrochemical flash sintering

Riku Fukada, [a] Claire V. Colin, [a] Timothée Fabre, [b] Marlu César Steil, [b] Renaud Bouchet [b] and Maria Diaz-Lopez *[a]

Electrochemical flash sintering (EFS) is a newly developed, solvent-free technique for ultrafast (~2 s) densification of lithium-containing solid-state battery materials. Unlike conventional flash sintering—which relies on uncontrolled thermal runaway and requires high electronic conductivity—EFS couples electronic conduction in mixed conductors with Li^+ transport across interfaces with pure ionic conductors in composite or multilayer architectures. Using spatially resolved synchrotron total scattering and pair distribution function analysis, we elucidate the mechanisms of EFS, contrasting them with conventional flash sintering of single-phase materials. Under conventional conditions, $Li_3V_2(PO_4)_3$ (LVP) undergoes localized decomposition and cracking at low frequencies and high currents, while $Li_{1.3}Al_{0.3}Ti_{1.7}(PO_4)_3$ (LATP) requires high frequencies to overcome blocking behavior—resulting in electrode melting, infiltration, and vitreous extrusion at the pellet perimeter. In contrast, EFS enables densification of LVP–LATP composites at lower frequencies that fail for either phase alone, with reactions confined to localized hotspots. In an LVP–LATP|LATP|LVP–LATP multilayer, decomposition products are more broadly distributed, including vanadium migration into the electrolyte; nonetheless, no preferential cracking or new phases were observed at electrode–electrolyte interfaces. These findings establish EFS as a viable one-step processing strategy for integrating (electro)chemically distinct phases and lay the groundwork for its broader adoption in the dry fabrication of solid-state electrochemical energy storage systems.

Received 5th January 2026
Accepted 4th April 2026

DOI: 10.1039/d6ta00082g

rsc.li/materials-a

Introduction

The electrification of transportation demands energy storage technologies that offer higher energy density, enhanced safety, and longer operational lifetimes than current lithium-ion batteries. All-solid-state lithium batteries (ASSLBs) have emerged as a leading candidate to meet these demands,[1] particularly for next-generation electric vehicles.[2] By replacing flammable liquid electrolytes with solid-state ionic conductors,[3,4] ASSLBs eliminate leakage and thermal runaway risks, greatly improving thermal and mechanical safety. Moreover, their potential compatibility with high-capacity lithium metal anodes[5] and wide electrochemical stability windows[6] open pathways to significantly greater energy densities.

Current ASSLB fabrication strategies rely on mechanical stacking of prefabricated electrode and electrolyte layers, followed by cold pressing or low-temperature annealing to establish interfacial contact.[7–10] These approaches often result in poor densification, poor interfacial adhesion, and high interfacial resistance, particularly in oxide-based systems.[11,12] This integration step remains a central bottleneck in the scalable manufacturing of ASSLBs, highlighting the need for alternative processing strategies that can simultaneously achieve intimate contact, chemical compatibility, and mechanical integrity across interfaces.[13]

A limited number of advanced sintering techniques have been explored to overcome the limitations of conventional high-temperature processing in ASSLB fabrication.[14–16] Among field-assisted techniques, spark plasma sintering (SPS)—also referred to as field-assisted sintering technology (FAST)—uses pulsed direct current (DC) and applied uniaxial pressure to achieve rapid densification at lower temperatures,[17,18] typically ~2/3 of conventional sintering at high temperature. SPS has been widely applied to solid electrolytes such as LLZO[19–22] and LATP,[23–26] achieving dense microstructures within minutes; however, its limited scalability and reliance on custom dies restrict its use in large-scale battery manufacturing. Solvent-mediated techniques, such as the cold sintering process (CSP), enable ceramic densification at temperatures below 300 °C by applying uniaxial pressures of 100–500 MPa in the presence of transient solvents. While CSP shows promise for the processing of composite[27] and hybrid solid electrolytes,[28] it has been rarely used for full solid-state battery stacking,[29] and its

[a]Institut Néel, CNRS, Universit, é, Grenoble Alpes, F-38042 Grenoble, France. E-mail: maria.diaz-lopez@neel.cnrs.fr
[b]Université Grenoble Alpes, Université Savoie Mont Blanc, CNRS, Grenoble INP, LEPMI, 38000 Grenoble, France

applicability to oxide-based systems is often limited by incomplete densification, residual solvent entrapment, and challenges in achieving phase purity.[30,31]

Our group recently introduced electrochemical flash sintering (EFS) as a novel processing route for integrating electrochemically active materials into ASSLB-type architectures (Fig. 1).[32] In our initial demonstration, EFS was successfully implemented in the fabrication of a symmetric all-solid-state cell, in which a composite $LiCoO_2$ (LCO) – $Li_{1.3}Al_{0.3}Ti_{1.7}(PO_4)_3$ (LATP) electrode was co-sintered with a central LATP electrolyte layer, forming an LCO–LATP|LATP|LCO–LATP monolithic structure with dense interfaces and no delamination. EFS builds on the principles of classical flash sintering (FS),[33,34] in which a ceramic body is simultaneously subjected to mild heating (typically 200–600 °C) and an external electric field—applied as DC or alternating current (AC)—to rapidly induce densification.[35–38]

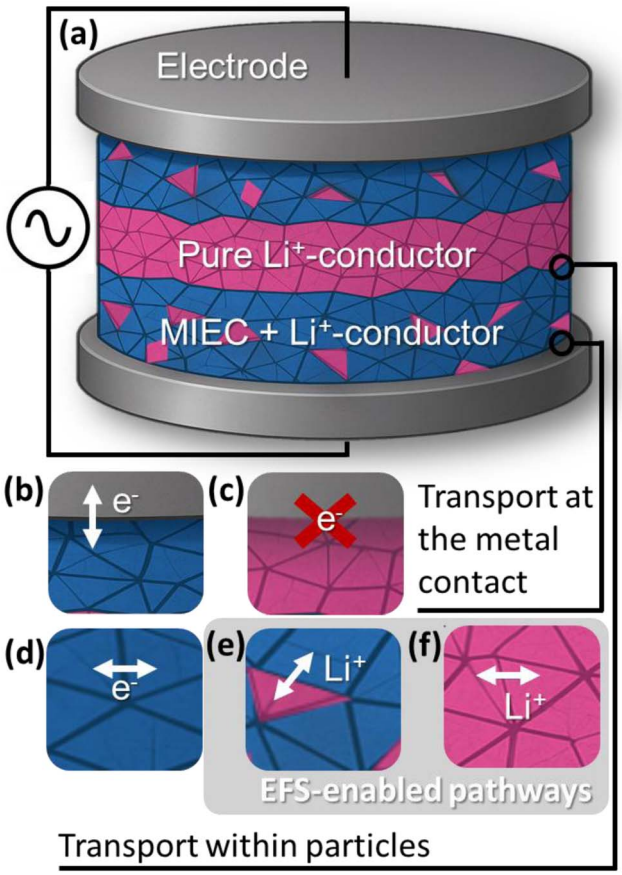

Fig. 1 Schematic representation of charge transport in EFS. (a) Symmetric multilayer consisting of composite electrodes formed from a mixed ionic–electronic conductor (MIEC, *e.g.*, LCO) and a purely ionic conductor (*e.g.*, LATP), separated by a central LATP electrolyte layer and subjected to an AC field between metal electrodes. Interfacial behavior at the metal contact: electron transfer occurs at metal–MIEC interfaces (b), but is blocked at metal–LATP interfaces (c). (d–f) In EFS, electron transport occurs through MIEC particles and is electrochemically converted at LATP interfaces into Li^+ conductivity, establishing new coupled electronic–ionic pathways. These pathways enable localized Joule heating and promote densification within electronically insulating regions.

Under DC conditions, the ceramic acts primarily as a resistive load, and Joule heating occurs through ohmic conduction. In materials with low electronic conductivity, DC-driven current is often hindered at grain boundaries or interfaces, where limited carrier mobility leads to charge accumulation[39] and non-uniform heating.[33,35,40,41] AC fields introduce frequency-dependent dielectric responses that, when sufficiently high (typically in the kHz-MHz range), suppress interfacial charge polarization. This improves dielectric losses and promotes more uniform Joule heating *via* both resistive and dielectric paths.[42] A demonstration of this is the five-order-of-magnitude increase in conductivity in hydroxyapatites by increasing the AC frequency to 1 MHz reported by Gittings *et al.*[43] Thus, tuning the AC frequency can unlock FS regimes in ion-blocking or highly resistive systems such as solid electrolytes.

Beyond frequency control, EFS introduces electrochemical functionality as a key driver of sintering. EFS applies to systems where mixed ionic-electronic conductors (*e.g.*, LCO) are coupled with purely ionic conductors (*e.g.*, LATP), either within intimately mixed composites or across stacked-layer configurations. The electronic conductivity in the mixed conductor facilitates electron flow, which in turn drives Li^+ migration into the adjacent ionically conducting domain, converting electronic conductivity into Li^+ transport (Fig. 1e and f). In composites, electrochemical charge redistribution occurs at the particle–particle interfaces; in layered stacks, it takes place across the electrode–electrolyte interfaces. In both cases, charge redistribution enables localized Joule heating and sintering even in the electronically resistive LATP.

Flash sintering of multilayered structures has also been explored in the context of solid oxide fuel cells (SOFCs), where mixed-conducting electrodes (*e.g.*, NiO–YSZ, LSM–YSZ) are coupled with a central oxide-ion conductor (*e.g.*, YSZ).[44,45] These studies demonstrated that FS could achieve densification without delamination; however, they focused primarily on thermal processing and did not investigate how asymmetric conduction, field distribution, or cation migration evolve under AC conditions. Moreover, while both O^{2-}- and Li^+-based systems rely on purely ionic conductors, Li^+ electrolytes like LATP often show lower overall conductivity at processing temperatures and greater chemical sensitivity to redox-driven decomposition and interfacial instability. These differences introduce new challenges and opportunities for flash processing of battery-relevant materials, where careful tuning of frequency, current, and layer geometry is required to control densification, minimize degradation, and maintain phase purity.[46]

Building on our previous demonstration of EFS in LCO–LATP|LATP|LCO–LATP multilayers, we now explore a more chemically compatible pairing. Although no secondary phases were observed during EFS, layered oxide cathodes like LCO are known to degrade over time when cycled with phosphate-based electrolytes, due to cobalt migration and resistive interphase formation.[47,48] To address this, we investigate $Li_3V_2(PO_4)_3$ (LVP)—a thermally stable, phosphate-based cathode with

improved compatibility with LATP, enabling long-term cycling stability in ASSLB architectures.[49,50] LVP crystallises in an *anti*-NASICON structure,[51] while LATP is a NASICON-type solid electrolyte.[52,53] Both share similar phosphate-based polyanionic backbones, which have been shown to reduce chemical reactivity at interfaces and suppress interdiffusion during high-temperature processing.[54–58] Given their shared phosphate backbone, LVP and LATP appeared to offer a more compatible pair for EFS-based densification—a hypothesis we critically evaluate in this work.

The transient nature of flash events, combined with steep thermal gradients and competing conduction mechanisms, makes it difficult to predict or control phase evolution, particularly in composite or multilayered architectures. In this work, we resolve the mechanisms of decomposition and phase redistribution that emerge under different sintering regimes—conventional (in single-phase LATP and LVP pellets) and electrochemical (in composite and multilayer stacks). Spatially resolved total scattering was employed to map structural and phase changes across pellet thickness, using both Bragg diffraction and pair distribution function (PDF) analysis to capture long- and short-range order in heterogeneous regions, revealing how local charge transport and redox processes govern thermal evolution and mechanical integrity during EFS. Despite these broader chemical transformations, interfacial contact between the layers remained mechanically intact, with no preferential cracking or accumulation of secondary phases at the electrode–electrolyte boundaries.

Together, these findings demonstrate that electrochemical charge redistribution during flash can be deliberately harnessed to promote densification and interfacial bonding between chemically distinct ASSLB-relevant materials. Whereas other field-assisted techniques—including SPS/FAST, microwave sintering,[59,60] and laser/photonic sintering[61–63]—can densify multilayer oxide systems, they require high uniaxial pressure, specialized tooling, vacuum environments, or induce widespread thermal and chemical gradients that accelerate interdiffusion. These constraints limit their applicability to scalable battery architectures. In contrast, EFS operates with simple, atmospheric-pressure hardware and enables localized, electrochemically guided heating that can decouple densification from extensive chemical degradation. With continued investigation into how geometry, field conditions, and mixed/pure Li^+-conductor pathways shape these reactions, EFS could emerge as a practical single-step, dry-processing strategy for reimagining interface processing in ASSLBs.

Results and discussion

The sintering conditions reported in this work produced dense pellets, with all samples achieving ≥85% relative density. Although effective for densification, certain sintering conditions led to non-uniform heating and current distribution, resulting in localized thermal hotspots that caused partial decomposition and the formation of secondary phases.[64] We systematically varied current density, frequency, incubation temperature, and post-flash hold time, combined with spatially resolved total scattering, to investigate the influence of processing parameters on material response.

The following sections present a system-by-system analysis of conventional FS—applied to single-phase LATP and LVP pellets to probe their intrinsic field and temperature responses—and EFS—applied to LVP–LATP composites and a multilayer LVP–LATP|LATP|LVP–LATP stack (Fig. 2). Experimental conditions and sample acronyms for all pellets are summarized in Table S1 (SI).

Conventional flash sintering of single-phase LATP

We first examined the flash sintering behavior of LATP. Unlike LVP, which supports mixed ionic–electronic conduction, LATP is a poor electronic conductor and exhibits strong blocking behaviour toward electronic current at low frequencies (*e.g.*, 1 kHz), thereby preventing flash onset. However, at higher frequencies (100–500 kHz), LATP can absorb energy from the alternating electric field through local displacements of Li^+ ions and polarization associated with Ti^{4+}/Ti^{3+} redox activity. These localized polarizable regions behave like transient dipoles that attempt to follow the rapidly oscillating field. As the frequency increases, their response becomes increasingly out of phase, and this lag leads to energy dissipation as heat, a process known as dielectric loss. As a result, dielectric heating becomes more pronounced at higher frequencies and contributes significantly to thermal input during flash sintering, even when the total current remains relatively low.

To investigate how field strength, frequency, and current control affect thermal input and electrode stability, two LATP samples were flash sintered under complementary conditions. LATP-4 A-100 kHz was processed at 250 °C with a pre-flash field of 200 V cm^{-1}, then transitioned to current control at 4 A cm^{-2}

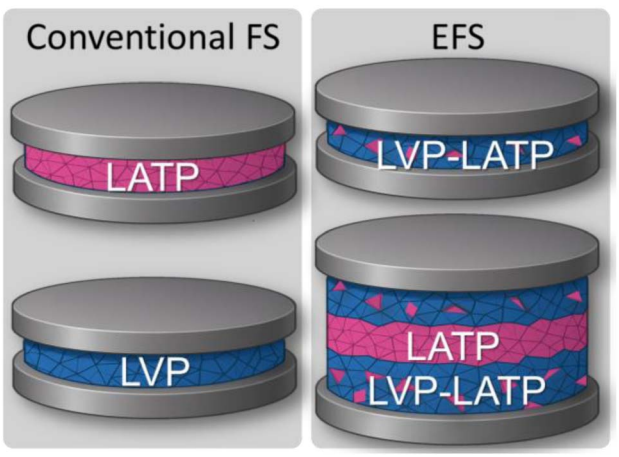

Fig. 2 Schematic representations of the four pellet architectures investigated. Single-phase LATP and LVP pellets (left) are subjected to conventional FS to probe their intrinsic field and temperature responses. In contrast, LVP–LATP composite pellets and the multilayer LVP–LATP | LATP | LVP–LATP stack (right) are processed using EFS, where MIEC pathways enable electronic–ionic coupling during flashing. Experimental conditions and sample acronyms for all pellets are provided in Table S1.

under 100 kHz AC using gold electrodes. LATP-300 V-500 kHz was sintered at 370 °C with a pre-flash field of 300 V cm^{-1}, followed by 3 A cm^{-2} current control at 500 kHz using platinum electrodes—chosen to better withstand the higher power input from increased field strength, frequency, and temperature. These conditions were designed to contrast a regime dominated by resistive heating (LATP-4 A-100 kHz: lower field, lower frequency, higher current density) with one favoring dielectric contributions (LATP-300 V-500 kHz: higher field, frequency, and temperature). Sample labels reflect the dominant control parameter during flash sintering: current density for LATP-4 A-100 kHz and applied field for LATP-300 V-500 kHz.

Localized temperatures during flash sintering exceeded the stability limits of both electrode materials, as evidenced by globules of molten metal embedded within the dense LATP matrix (Fig. 3). This indicates melting, migration, and recrystallization of Au electrodes under resistive conditions—and even of Pt under dielectric-heating conditions—despite the latter's significantly higher melting point (~1768 °C *vs.* ~1064 °C for Au).

Beyond electrode migration, the LATP-4 A-100 kHz sample appeared uniformly dense with no visible colour gradients. In LATP-300 V-500 kHz, a bluish tint was observed, indicative of titanium in mixed oxidation states (Ti^{3+}/Ti^{4+}), along with a vitreous, metallic-looking perimeter. Because LATP did not display the spatial features characteristic of hotspot-driven decomposition, spatially resolved scans across the pellet (as performed for LVP and composite pellets in the following sections) were not applicable. Instead, the analysis focused on comparing the microstructure and crystallinity between the central ceramic region and the outer vitrified zone, as shown in Fig. 3.

The LATP-4 A-100 kHz pellet shows minimal evidence of decomposition, with only minor secondary phases such as

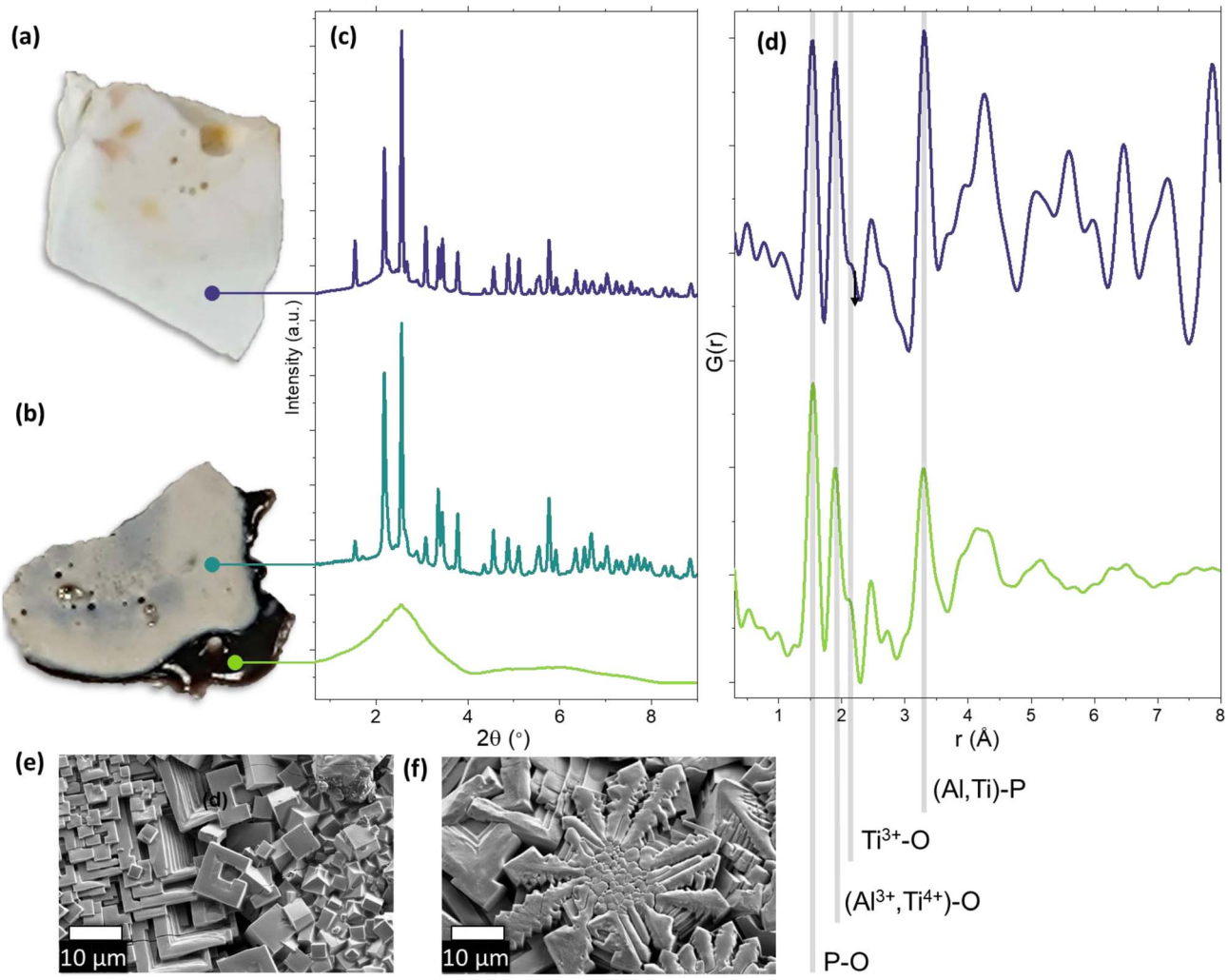

Fig. 3 (Micro)structure of flash-sintered LATP (a) LATP-4 A-100 kHz and (b) LATP-300 V-500 kHz pellets after flash sintering, showing visible electrode migration. Discoloration and embedded metallic globules correspond to the inward diffusion and melting of Au (a) and Pt (b) electrodes. (c) X-ray diffraction patterns and (d) PDFs collected from selected regions of each pellet highlight the presence of both crystalline and amorphous domains. (e,f) SEM images of the white ceramic (non-vitreous) region of LATP-300 V-500 kHz reveal well-developed, faceted grains with distinct morphologies.

$AlPO_4$ and possibly Li_3PO_4 or $LiTiOPO_4$ detected by powder diffraction (Fig. 4).[65,66] In contrast, LATP-300 V-500 kHz exhibits pronounced differences in crystallinity between its white ceramic core and vitreous periphery, as shown in Fig. 3. Diffraction patterns collected from the ceramic region in LATP-300 V-500 kHz confirm the presence of LATP as the primary phase, though variations in relative peak intensities suggest pronounced preferred orientation. SEM analysis of this region (Fig. 3e and f) reveals a diverse population of crystal morphologies—including well-faceted cubic grains and more dendritic forms—indicative of multiple growth regimes during rapid quenching.

To capture the resulting anisotropy in the diffraction pattern, a spherical harmonics model was employed in the Rietveld refinement. While the extracted texture terms do not correspond to a single crystallographic orientation, they successfully account for the complex intensity variations arising from the coexistence of distinct grain morphologies observed by SEM (Fig. 3). Additionally, the refinement revealed a greater concentration of secondary phases compared to the lower-frequency LATP-4 A-100 kHz sample: $AlPO_4$ (6.3 wt%), $LiTiOPO_4$ (2.8 wt%), and Li_3PO_4 (2.1 wt%).

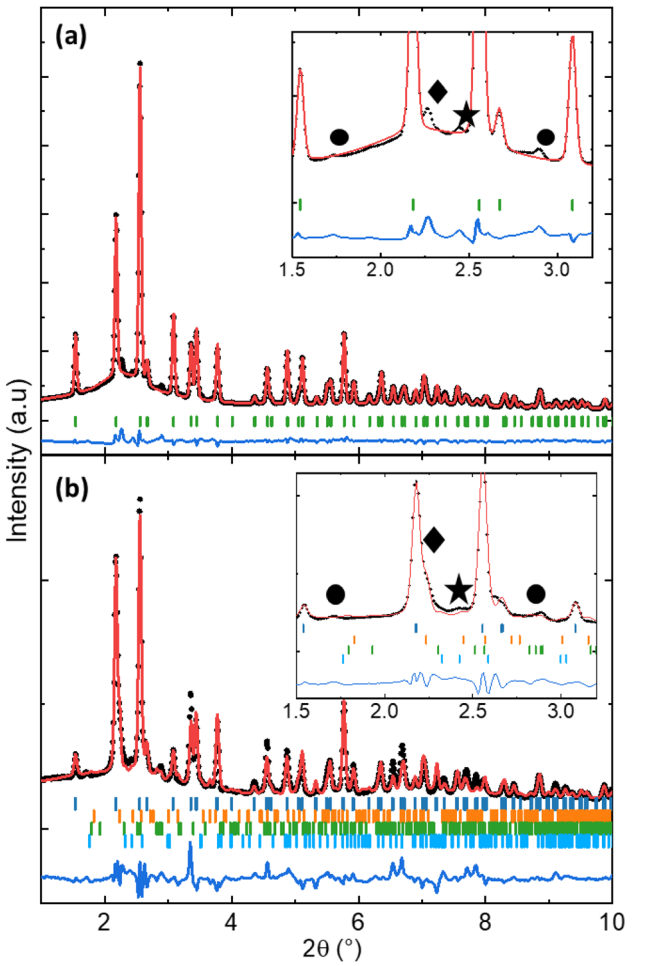

Fig. 4 Rietveld refinement of LATP-4 A-100 kHz (a) and LATP-300 V-500 kHz (b). Experimental data (black), calculated fit (red), and difference pattern (blue, bottom) are shown, with vertical green ticks marking Bragg positions for the LATP phase. The inset highlights minor impurity peaks assigned to $AlPO_4$ (◆, $C222_1$), $LiTiOPO_4$ (●, *Pnma*), and Li_3PO_4 (★, *Pmnb*). Refined lattice parameters and fit statistics are provided in Table S2.

In reciprocal space, the diffraction data from the vitreous boundary region of the LATP-300 V-500 kHz sample show no well-defined Bragg peaks, indicating a substantial loss of long-range crystallinity. Complementary real-space PDF analysis reveals a lack of atomic correlations beyond ~7 Å, consistent with severely limited structural coherence. This degree of amorphization likely results from localized overheating—exceeding 1700 °C, as suggested by partial Pt electrode melting—followed by rapid quenching. Together, these conditions promote structural collapse and vitrification at the pellet's outer rim.

Additionally, PDF analysis of the vitreous boundary region in LATP-300 V-500 kHz reveals an increased contribution from Ti^{3+}, evidenced by the enhanced intensity of the Ti^{3+}–O peak—already present in the unsintered LATP precursor (Fig. S1)—and a concurrent reduction in the relative intensity of the Ti^{4+}/Al^{3+}–O peak compared to that of P–O. The resulting amorphous Ti^{3+}-rich phase may compromise the electrochemical and mechanical integrity of the pellet, highlighting the importance of controlling thermal gradients during flash sintering.

Both sintering conditions yielded dense ceramics, with LATP-4 A-100 kHz exhibiting higher phase purity, indicating that 100 kHz was sufficient to overcome the low electronic conductivity of LATP and enable densification. Previously reported electrochemical impedance spectroscopy on the phase-purer LATP-4 A-100 kHz sample further showed that flash-sintered single-phase LATP remains ionically conductive, with an activation energy of ~0.25 eV and room-temperature conductivity in the expected range for dense LATP, confirming that the material remains electrochemically functional under these processing conditions.[32] While higher frequencies are necessary to overcome interfacial electronic blocking, operation at 100 kHz also produced intense, localized heating near the metal–ceramic contact. This arose from two effects: (1) electric-field intensification at microscopic contact points between LATP and the electrode, where dielectric heating—scaling with the square of field strength—induces sharp local temperature rises; and (2) interfacial impedance, originating from charge accumulation at the electronically/ionically mismatched boundary, which further dissipates energy as heat. Together, these effects generated temperature spikes high enough to melt Au and even Pt electrodes in LATP-300 V-500 kHz, showing that while higher frequencies improve densification and phase purity, they also promote severe interfacial heating. In contrast, at 1 kHz no flash onset was observed, confirming that a minimum frequency threshold is required for activation.

Thus, the optimal processing window for single-phase LATP is narrow, lying between 1 kHz, below which flash cannot be initiated, and 100 kHz, where excessive interfacial heating occurs. This narrow frequency–temperature window stems from the low electronic conductivity of LATP, and underscores the limitations of conventional flash sintering for purely ionic conductors. These constraints motivate the exploration of EFS,

where the inclusion of a mixed-conducting phase redistributes charge and drives Li^+ transport, enabling more uniform thermal profiles.

Conventional flash sintering of single-phase LVP

To understand how LVP responds to flash sintering, we explored varying current densities and field frequencies. Five LVP pellets were processed under fixed incubation conditions (300 °C for 50 s), while systematically adjusting the applied current density (2, 6, 7.5, and 9 A cm^{-2}) and frequency (1 kHz or 100 kHz). Specifically, LVP-2 A-1 kHz, LVP-6 A-1 kHz, LVP-7.5 A-1 kHz and LVP-9 A-1 kHz differ only in current, allowing a direct comparison of current effects. LVP-6 A-100 kHz isolates the influence of frequency.

Photographs for these samples and corresponding spatially resolved diffraction through the pellet thickness are presented in Fig. 5 and S2. Hotspot formation was observed in all pellets except LVP-6A-100 kHz, which showed a more uniform appearance, suggesting a different thermal evolution pathway at higher frequencies.

Upon FS, the initially light-grey LVP powder underwent distinct color changes, producing a consistent three-zone morphology across most samples. These visual patterns indicate localized thermal gradients and the formation of a central hotspot. The innermost region, or hotspot core, appeared grey with yellow highlights and marks the area of peak temperature, evidenced by localized melting of the Au electrode during flash, indicating that this region exceeded ~1064 °C, while the rest of the pellet remained below this temperature. Surrounding this core is a yellow annular region, denoted as the intermediate zone, which transitions outward into a darker grey rim at the pellet edge—the peripheral zone. The visual contrast between these regions reflects spatial variations in heating history and reaction extent, and correlates with the structural changes identified through diffraction mapping, discussed in detail below.

The consistent appearance of these zones on both the top and bottom surfaces of the pellets suggests that the hotspot spans the full pellet thickness (Fig. 5a–d). To verify this, sample LVP-7.5 A-1 kHz was sectioned, and XRD data were collected laterally across part of its cross-section (Fig. S2), confirming that the three-zone morphology extends through the full ~2–3 mm thickness.

Non-negative matrix factorization (NMF)[67] was applied to diffraction data in both reciprocal (Bragg) and real space (PDF) to provide an unbiased assessment of the phases present across the heterogeneous flash-sintered pellets. This approach enabled us to identify the minimum number of structural components required to describe the data and to isolate their contributions for subsequent phase identification. In reciprocal

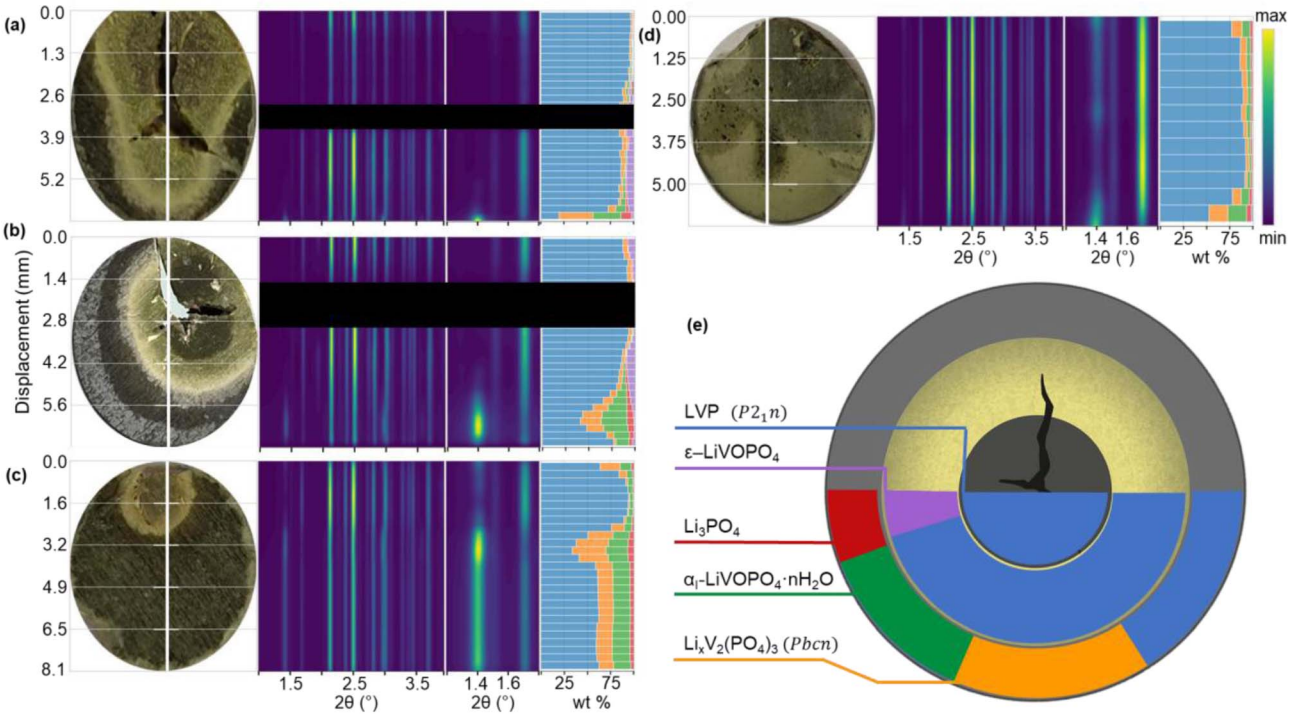

Fig. 5 Structural evolution of LVP under varying FS conditions. (a) LVP-9 A-1 kHz (b) LVP-6 A-1 kHz (c) LVP-2 A-1 kHz (d) LVP-6 A-100 kHz. Optical images (left), 1D X-ray diffraction heatmaps across the pellet thickness (center), phase quantification by Rietveld refinement (right). (e) Schematic phase distribution highlighting three reaction zones: hotspot core (center), intermediate, and peripheral decomposition zones. Five major crystalline components are identified and included in the Rietveld refinements: $Li_3V_2(PO_4)_3$ ($P2_1/n$), ε-$LiVOPO_4$, Li_3PO_4, and $Li_xV_2(PO_4)_3$ ($Pbcn$) and α_I-$LiVOPO_4 \cdot nH_2O$. Three concentric regions are identified based on visual and structural features: hotspot core (dark grey), intermediate (yellow), and peripheral zones (grey). Note that the pellet in (a) was digitally rescaled along one axis for layout consistency; all pellets were originally round.

space, iterative analysis showed that three components best captured the Bragg features (Fig. 6). In real space, two components were identified due to the similarity of local interatomic distances among the phases. No additional components were necessary, indicating the absence of amorphous phases from FS-induced vitrification.

Complementary higher-resolution diffraction was performed on powders prepared by breaking the sintered pellets and grinding material from each visually distinct region. ε-$LiVOPO_4$, Li_3PO_4, α-$LiVOPO_4 \cdot nH_2O$, and $Li_xV_2(PO_4)_3$ with $x > 2.5$ were identified as secondary phases formed due to lithium redistribution and partial decomposition driven by the strong thermal gradients during flash. Rietveld refinement was used to extract lattice parameters (Fig. S3, Table S3) and phase fractions (Fig. 5), providing quantitative insight into the extent of reaction across FS-ed pellets.

As shown in Fig. 5 and S2 LVP-2 A-1 kHz, LVP-6 A-1 kHz, LVP-7.5 A-1 kHz, and LVP-9 A-1 kHz pellets show a well-defined three-zone structure. The hotspot core—corresponding to the region of highest current density—primarily consists of phase-pure, unreacted LVP. However, mechanical integrity is compromised, especially at higher current densities (6 and 9 A cm^{-2}), due to the formation of cracks driven by steep thermal and stress gradients during flash events.

The microstructural effects of localized thermal gradients during flash sintering were examined by SEM for sample LVP-4 A-1 kHz (Fig. 7). The hotspot region exhibits extensive grain coarsening and near-complete densification, along with rounded, intergranular inclusions that are consistent with Au infiltration from the electrode. This is supported by visible deformation and localized melting of the gold layer at the pellet center, where the temperature likely exceeded the Au melting point (~1064 °C). In contrast, the intermediate and peripheral zones display finer grains, intergranular porosity, and less uniform morphology—features indicative of lower local temperatures and incomplete sintering. The spatial gradient in grain size and microstructure aligns with the three-zone thermal model developed from diffraction and optical observations. The distinct microstructural transitions provide direct evidence of steep internal thermal gradients that drive both localized densification and decomposition in LVP during conventional FS.

Despite experiencing the highest instantaneous temperatures, the hotspot remains largely phase-pure LVP. This likely results from the extremely rapid heating and densification during flash, which favors fast sintering *via* grain boundary diffusion over slower processes like delithiation or rearrangement of the phosphate framework. Additionally, thermal shock and cracking in this region may disrupt transport pathways, suppressing phase transformations despite extreme local conditions. The surrounding material may also act as a chemical buffer, limiting the escape of volatile lithium and phosphorus species and thereby further stabilizing LVP in this zone. This may explain why the hotspot remains phase-pure, while peripheral regions—subject to slower heating—are more susceptible to lithium redistribution and secondary phase formation, as discussed below. Moving outward from the hotspot, the intermediate zone contains the oxidized ε-$LiVOPO_4$

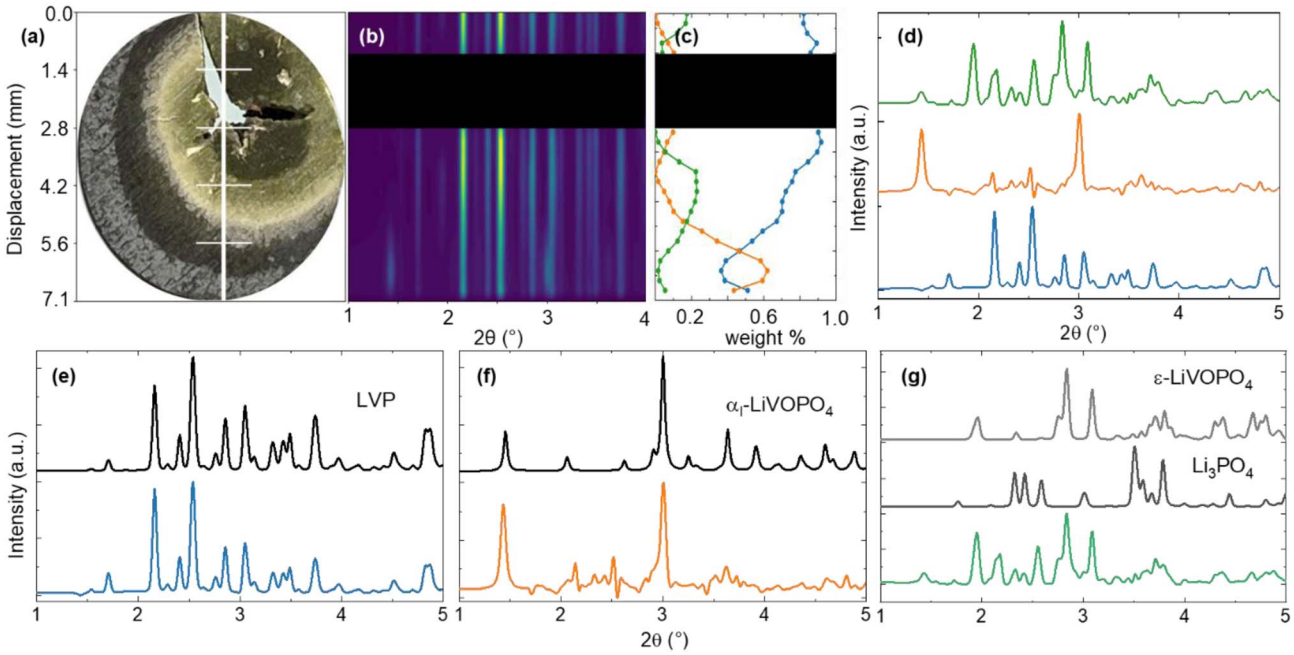

Fig. 6 Elucidating phase components in a flash-sintered LVP pellet using spatially resolved synchrotron XRD and NMF. (a) Picture of the pellet after EFS, showing a central hotspot and radial crack. The vertical white line marks the XRD scan path. (b) Spatially resolved XRD patterns along the scan path; the blacked-out region corresponds to signal loss at the crack location. (c) Relative weight fractions of the three NMF-extracted components. (d) NMF-extracted diffraction patterns, color-matched to the curves in (c). (e–g) Comparison of NMF components with simulated reference patterns for LVP, α-$LiVOPO_4$, ε-$LiVOPO_4$, and Li_3PO_4.

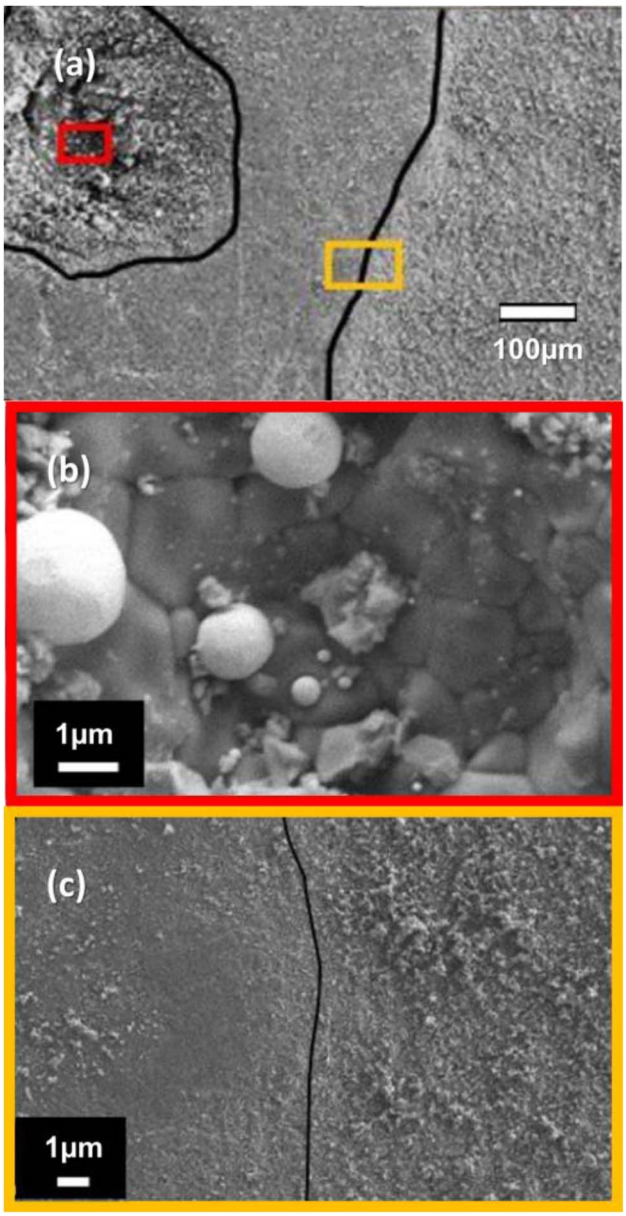

Fig. 7 Microstructural characterization of LVP–4 A–1 kHz by SEM. (a) Overview image of the hotspot morphology. Black solid lines denote the boundaries between the hotspot core, intermediate, and peripheral zones. Red and yellow boxes indicate the locations of the higher-magnification images in (b) and (c), respectively. (b) Hotspot core region, exhibiting significant grain coarsening and near-complete densification. Smooth, rounded inclusions are observed, likely resulting from localized melting and infiltration of molten Au from the electrode. (c) Transition region at the boundary between the intermediate and peripheral zones, showing finer grains and residual porosity, consistent with lower peak temperatures and incomplete sintering.

phase. While previous studies have shown that LVP is highly sensitive to oxygen—reporting that even ~5 ppm O_2 can cause peak broadening due to trace oxidation—such low O_2 content cannot explain the extent of phase transformation observed.[68] Instead, the formation of ε-$LiVOPO_4$ is more plausibly attributed to thermally driven reactions activated under the intense local heating during the flash. A decomposition pathway consistent with the formation of ε-$LiVOPO_4$ is given by:

$$Li_3V_2(PO_4)_3 \rightarrow 2\varepsilon\text{-}LiVOPO_4 + 1/2Li_2O + 1/2P_2O_3 \quad (1)$$

This reaction includes volatile byproducts (Li_2O and P_2O_3), which are not detected crystallographically but are required for elemental balance. These species are expected to be released during rapid thermal decomposition under non-oxidizing conditions.[69,70]

Out of the two $LiVOPO_4$ polymorphs identified, only the ε-polymorph was observed in the reaction zone. This is consistent with ε-$LiVOPO_4$ forming *via* topotactic delithiation of LVP under rapid, localized thermal gradients—a mechanism favored by the structural similarity between LVP and the ε-phase, which allows lithium extraction without major rearrangement. Under such kinetically constrained conditions, the system lacks sufficient time to evolve into more thermodynamically stable polymorphs like β-$LiVOPO_4$.

The hydrated α_I-$LiVOPO_4$ polymorph, exhibiting limited structural coherence, was identified in the peripheral region of the pellet (Fig. S3). Hydration occurred post-sintering[71] as demonstrated by subsequent heat treatment (>200 °C) or vacuum drying fully reverting to anhydrous α_I-$LiVOPO_4$, which in turn rehydrated in ambient conditions over the course of two months (Fig. S4, S5). Variable-temperature XRD shows α_I-$LiVOPO_4 \cdot nH_2O$ dehydrates and transforms into ε-$LiVOPO_4$ upon heating, confirming that the phase identified as α_I is indeed a polymorph of $LiVOPO_4$.

The peripheral zone also contains the partly oxidized orthorhombic $Li_xV_2(PO_4)_3$ phase (space group *Pbcn*), typically reported for $x \approx 2.5$.[72] However, the lattice parameters refined in this work ($a = 8.5983\ (7)$Å, $b = 8.6259\ (7)$ Å, $c = 12.1547\ (10)$ Å) are larger than those reported for $Li_xV_2(PO_4)_3$ at $x \approx 2.5$ ($a = 8.5539\ (4)$ Å, $b = 8.6099\ (4)$ Å, $c = 11.9825\ (5)$ Å) and more closely resemble values observed in Zr-doped or partially sodiated analogs.[73,74] Thus, FS conditions stabilized this structure at a higher lithium content.

In addition to $Li_xV_2(PO_4)_3$ and αI-$LiVOPO_4 \cdot nH_2O$, the peripheral decomposition zone also contains Li_3PO_4 at low concentrations. This is consistent with the outward diffusion of Li_2O and P_2O_3 during decomposition in eqn (1), followed by recombination with trace O_2 (~5 ppm) present in the nominally inert Ar atmosphere at the cooler pellet edge:

$$3Li_2O + P_2O_3 + O_2 \rightarrow 2Li_3PO_4 \quad (2)$$

In LVP-2 A-1 kHz, a localized hotspot developed near the center of the pellet, which otherwise remained mechanically intact and showed no visible cracking—unlike samples sintered at higher current densities (6, 7.5, and 9 A cm^{-2}). ε-$LiVOPO_4$ was not detected by diffraction, indicating that the current density was insufficient to generate the peak temperatures required for its formation. However, the overall concentration of $Li_xV_2(PO_4)_3$ (*Pbcn*), αI-$LiVOPO_4 \cdot nH_2O$, and Li_3PO_4 is higher in LVP-2 A-1 kHz compared to LVP-(6 and 7.5)A-1 kHz, and lowest in LVP-9 A-1 kHz, as shown by the refined phase fractions in Fig. 5. This

trend suggests that lower current densities, while avoiding mechanical damage, promote more extensive peripheral decomposition. In contrast, higher current densities result in larger phase-pure LVP cores, but compromised mechanical integrity due to cracks formed by steep thermal gradients.

At a fixed current density of 6 A cm^{-2}, increasing the frequency from 1 kHz to 100 kHz (sample LVP-6A-100 kHz) resulted in no visible hotspot formation or cracking, and the pellet remained mechanically intact. Although decomposition products such as $Li_xV_2(PO_4)_3$ (*Pbcn*), α_I-$LiVOPO_4 \cdot nH_2O$, and Li_3PO_4 were still detected, their refined weight fractions were lower than in LVP-6 A-1 kHz, and ε-$LiVOPO_4$ was absent. The phase distribution in Fig. 5d reveals a predominantly phase-pure LVP pellet with only narrow decomposition zones near the periphery.

These results suggest that higher frequencies do not significantly shift the flash onset but alter how the flash develops spatially. At 100 kHz, the applied electric field appears more uniformly distributed across the sample, reducing the formation of sharp thermal gradients that typically drive hotspot formation and cracking. Although phase decomposition still occurs, it is more diffuse and less severe, as indicated by the broader distribution and lower overall concentration of secondary phases. This points to a fundamentally different mode of thermal activation—less abrupt, more spatially extended, and potentially easier to control. Similar frequency-dependent homogenization of thermal profiles has been reported for purely ionic conductors such as LLZO[75] and 8YSZ,[76] while pure electronic conductors show little change in onset with frequency.[76] The mixed ionic–electronic character of LVP may therefore confer partial dielectric response enabling heat dissipation and improved spatial uniformity at high-frequency fields.

Thus, frequency acts as a temporal and spatial modulator of thermal profiles during the flash sintering of mixed-conducting materials, influencing the extent of phase decomposition and mechanical integrity of the sintered pellets. This frequency-dependent behavior highlights the role of electrochemical reactions even during conventional flash sintering of single-phase materials. In the following sections, we deliberately exploit these reactions by spatially combining mixed and purely ionic conductors in composite and multilayer architectures under EFS conditions.

Electrochemical flash sintering of LVP–LATP composites

When the NASICON framework of LATP is co-sintered with phosphate-based electrodes such as $LiFePO_4$ or $LiCoPO_4$ above 700 °C, the interdiffusion of transition metal ions can lead to a transformation from the rhombohedral NASICON framework to orthorhombic *anti*-NASICON phases.[54,55,77,78] We therefore evaluated the reactivity of a mixed LVP : LATP powder mixture in 6 : 4 ratio (by weight) under standard sintering conditions at 700 °C, 750 °C, and 800 °C for 3 hours to determine the onset and extent of interphase transformations (Fig. 8). Post-annealing powder X-ray diffraction revealed the formation of a new orthorhombic *anti*-NASICON phase (*Pbna*), attributed to Al and Ti incorporation from LATP into the LVP lattice. Rietveld refinement showed that even at 700 °C, 86.8 wt% of the material had transformed into this Ti,Al-doped LVP phase. The transformation progressed to 98.6 wt% at 750 °C and was complete by 800 °C, yielding a refined composition of $Li_2Al_{0.15(2)}V_{0.77}Ti_{1.08(2)}(PO_4)_3$ (theoretical composition $Li_{2.02}Al_{0.24}V_{0.77}Ti_{0.99}(PO_4)_3$). Full refinement details are provided in Fig. S6 and Tables S4–S5.

Seeking to balance composite densification with chemical compatibility, we investigated two key EFS parameters: AC field frequency and the introduction of a post-flash current hold. As for single-phase FS, frequency was varied to evaluate the effect of dielectric heating on LATP and spatially redistribute heating, reducing thermal gradients. The post-flash current hold extends the high-temperature window following the initial flash, potentially allowing additional densification and gaining control during grain growth and structural relaxation at LATP–LVP interfaces.

The sintered LVP–LATP composites consistently exhibit a three-zone hotspot morphology, comprising a dark brown core (distinct from the grey and white appearance of the pristine LVP and LATP powders, respectively), an orange intermediate zone, and a pale grey peripheral rim. This evolution is most clearly seen in samples composite-6 A-1 kHz-0 s and composite-6 A-1 kHz, which were processed under identical current density (6 A cm^{-2}) and frequency (1 kHz), but with differing post-flash hold times (0 and 50 s; see Fig. S7). Increasing the hold time visibly expands the extent of the transformed core region and induces mechanical damage; composite-6 A-1 kHz fractured along the hotspot core following the 50 s current hold. To enable spatially resolved structural analysis, this sample was fractured post-sintering, and each region was independently analyzed by powder X-ray diffraction (Fig. S7, Table S6).

Quantitative Rietveld refinement revealed that the hotspot core predominantly consists of a Ti, Al-substituted LVP phase (62 wt%), with minor fractions of unreacted LATP (15 wt%) and LVP (23 wt%). At higher frequencies, the reacted phase exceeds 90 wt%, correlating with the broader extent of the transformed hotspot core. The intermediate zone displays a mixture of the reacted phase with residual LATP and LVP. In the peripheral rim, phase decomposition products such as α_I-$LiVOPO_4 \cdot nH_2O$ and Li_3PO_4 are observed, consistent with previously established decomposition pathways (eqn (1) and (2)). Notably, these decomposition products are present even in the absence of a post-flash hold, indicating that their formation is primarily driven by the electric field during flash onset, rather than sustained heating. The introduction of a current hold at 1 kHz extends the decomposition by enlarging the hotspot core region. However, in regimes where hotspot formation can be minimized—such as at higher frequencies of 100 kHz in single-phase LVP—this approach may still prove beneficial.

The evolution of hotspot morphology with frequency was examined *via* 1D X-ray diffraction scans across the pellet cross-sections (Fig. 9). At 1 kHz (composite-6 A-1 kHz), the reaction between LATP and LVP was confined to the small hotspot core region, while the rest of the pellet was dense and primarily composed of unreacted LATP and LVP with minor (5 wt%)

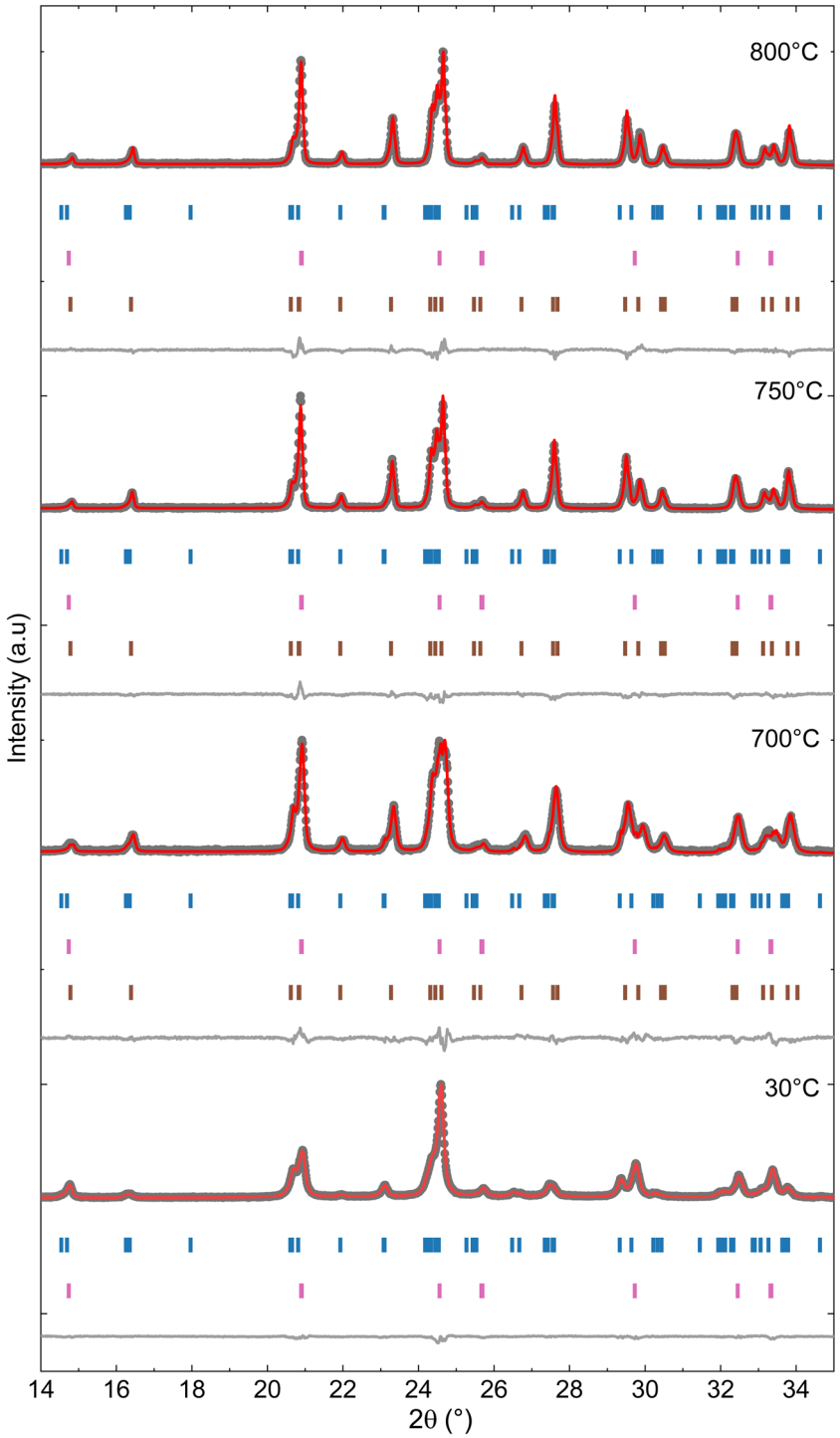

Fig. 8 X-ray diffraction data of LATP : LVP composites measured at room temperature for the ball-milled powder and conventionally sintered pellets annealed under Ar at 700, 750, and 800 °C for 3 hours. Vertical tics indicate the Bragg position of LVP (blue), LATP (pink), and (Al-Ti)-doped LVP (brown). During refinement, the lattice parameters of the LVP and LATP phases were fixed to values obtained from the corresponding pure-phase reference samples.

decomposition phases—in stark contrast to >85 wt% secondary phases formed by conventional sintering at only 700 °C. Increasing the frequency to 100 kHz produced two distinct hotspots, each showing near-complete reaction between LATP and LVP. At 200 kHz (composite-6A-200 kHz, Fig. S8), flash propagation appeared less uniform, with visually heterogeneous coloration and no concentric zoning. The sample transitioned from its original grey tone to an orange-brown body with blackened regions and localized surface melting, including a blob of expelled material. Despite the irregular morphology,

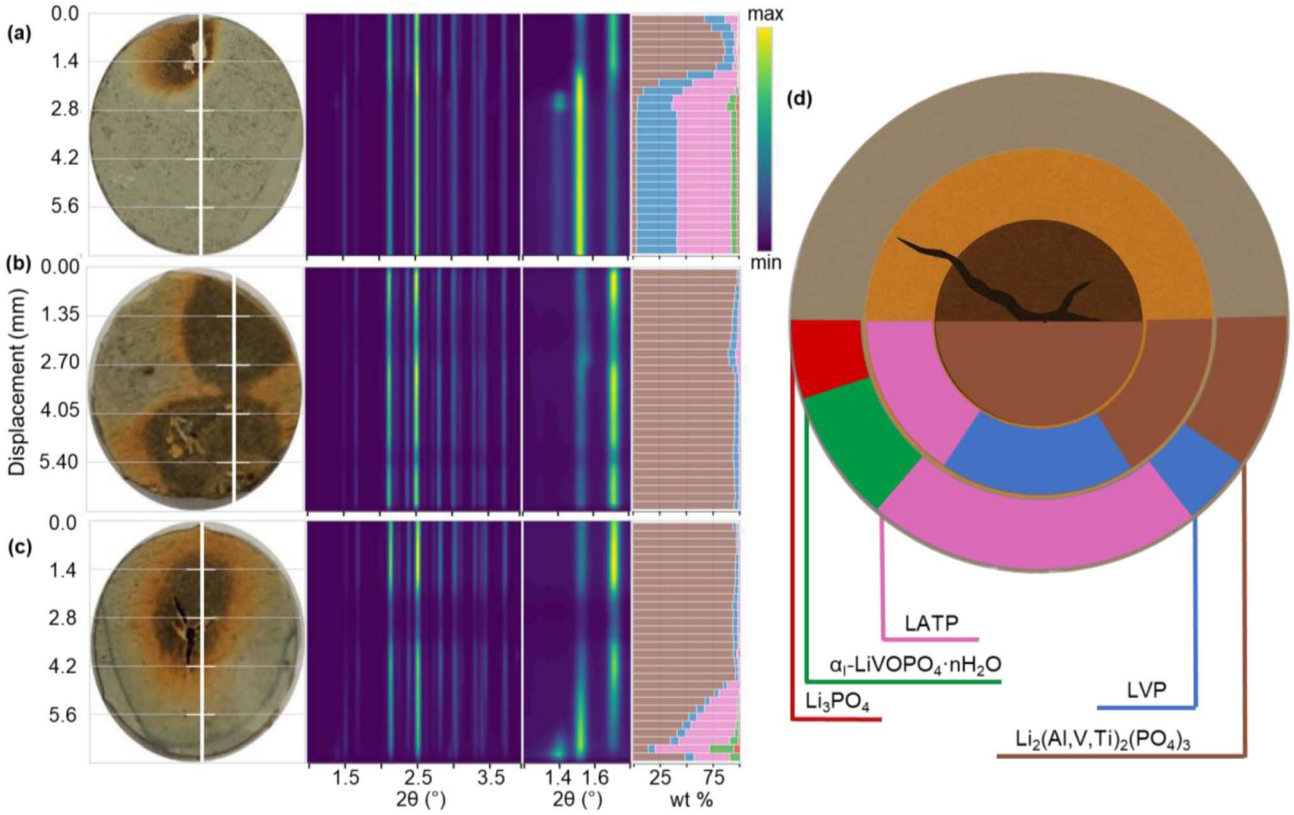

Fig. 9 Structural evolution of LATP–LVP composite pellets under varying EFS conditions. (a) Composite-6A-1kHz-0s, (b) Composite-6A-100 kHz, (c) Composite-6A-300 kHz. Optical images (left), 1D X-ray diffraction heatmaps across pellet thickness (center), and corresponding phase quantification by Rietveld refinement (right). In all samples, sintering was performed at 6 A cm^{-2} and 300 °C with varying AC frequency and current hold times; sample (c) only reached 3 A cm^{-2}. (d) Schematic representation of composite pellets illustrating the spatial distribution of major crystalline phases: $Li_3V_2(PO_4)_3$, α_l-$LiVOPO_4 \cdot nH_2O$, Li_3PO_4, $Li_{1.4}Al_{0.4}Ti_{1.6}(PO_4)_3$, and the $Li_2(Al, V, Ti)_2(PO_4)_3$. Three concentric regions are identified based on visual and structural features: hotspot core (dark brown), intermediate zone (orange), and peripheral region (grey).

three structurally distinct zones were isolated around the central fracture and analyzed as powders (Fig. S8, Table S7). These showed varying degrees of reaction and decomposition.

Composite-6A-300 kHz marked the upper limit of our frequency range. The pellet failed to reach the target current density of 6 A cm^{-2}, plateauing at ~3 A cm^{-2}. The suppressed current is likely due to increased inductance at higher frequencies, which limits current flow and reduces flash intensity. As a result, the thermal impact was lower than in Composite-6A-200 kHz. Still, substantial LATP–LVP reaction, Li_3PO_4 and α_l-$LiVOPO_4 \cdot nH_2O$ were found in the intermediate and peripheral zones, demonstrating that LVP decomposition can proceed even under weaker current input.

Unlike in conventional FS of single-phase LVP, the LVP phase in the composite does not undergo oxidation to ε-$LiVOPO_4$. In the single-phase system, localized lithium depletion during flash sintering drives V^{3+} oxidation to V^{4+}, promoting the formation of ε-$LiVOPO_4$. In the composite, the incorporation of LATP introduces an extended Li^+ transport network that redistributes the electric field more uniformly. This mitigates steep local gradients in lithium chemical potential, suppresses localized oxidation, and stabilises the phase purity of LVP. As a result, low-frequency operation at 1 kHz—which produced poor outcomes for both single-phase LATP and LVP—yielded the most favorable result in the composite, with minimal phase degradation outside the hotspot. These findings highlight how phase composition and ionic transport pathways can work synergistically to stabilize composite systems under *electrochemical* FS conditions.

Electrochemical flash sintering of a monolithic LVP–LATP|LATP|LVP–LATP multilayer

A symmetric LVP–LATP|LATP|LVP–LATP multilayer was flash sintered at 485 °C under a 6 A cm^{-2} AC (1 kHz) with a 50 s post-flash hold, using the frequency and current densities that produced the best results in composites, though retaining the 50 s post-hold previously associated with greater decomposition. The resulting monolith measured 8 mm in diameter and approximately 5 mm in thickness—dimensions chosen to amplify thermal and electrochemical gradients and expose the underlying mechanisms governing EFS-driven densification and phase evolution. While thinner, application-relevant multilayers can be sintered with minimal cracking, the present study focuses on capturing the evolution of thermal and electrochemical processes that define EFS, rather than optimizing electrochemical performance.

Despite the formation of several longitudinal and transverse cracks (Fig. 10a and b), the sintered body remained mechanically self-supported. The pellet was sectioned into three parts for structural analysis (overview in Fig. S9), and total scattering experiments were performed on each section, with the central segment scanned from top to bottom at three distinct positions exhibiting varying degrees of densification—from the most densified region (Fig. 10e) to the least (Fig. 10c). Analyses of the outer segments are presented in the SI (Fig. S10–S11).

Aside from mechanical cracking, the composite layers changed in colour, turning brown—similar to the hotspot cores observed in EFS-processed composite pellets. XRD analysis revealed that these brown regions were predominantly composed of Al, Ti-doped LVP, with concentrations ranging from ~20 wt% in densified regions away from the electrode–electrolyte interface (Fig. 10e) increasing to ~42 wt% closer to the interface. In less densified regions, the Al, Ti-doped LVP formed at a greater proportion, reaching a maximum of ~89 wt% near the interface (Fig. 10c and d). 5–8 wt% Al, Ti-doped LVP was also detected in the nominally pure LATP electrolyte layer, of over 1 mm in thickness. The extent of migration of V^{3+} (and possibly V^{4+}) cation across several hundred microns into the pure LATP electrolyte layer is surprising under AC fields, which reverse direction too rapidly to support long-range, directional transport. Thus, other factors such as high local temperatures and enhanced diffusion pathways may have overcome this effect.

ε-$LiVOPO_4$ was also detected throughout the composite layers. Its concentration was highest in the outer pellet sections (~30 wt%, Fig. S10), decreasing toward ~25 wt% at the outer surface of the middle section (Fig. 10), and as low as ~15–20 wt% near the electrode–electrolyte interface. Unlike in single-phase LVP where ε-$LiVOPO_4$ was primarily localized in the intermediate zones surrounding hotspot core at lower concentrations (~5–7.5 wt%) or composite-only systems, where this phase was absent, ε-$LiVOPO_4$ is present at significantly higher concentrations and across all regions of the composite within the multilayer. This widespread formation indicates that the thermal threshold for LVP decomposition in eqn (2) was exceeded. Furthermore, the formation of ε-$LiVOPO_4$ may have been promoted by prolonged heating, which has been shown to favor the stabilization of this polymorph at the intermediate zone in single-phase LVP, while being suppressed at the hotspot core, where rapid heating and cooling rates dominate.

In contrast to the relatively uniform field distribution in single-phase or fully composite pellets, the layered geometry of the multilayer introduces spatial heterogeneity in both Li^+ migration and Joule heating. This can result in localized regions of elevated temperature at specific depths within the pellet. Gradients in ionic mobility and charge accumulation at the

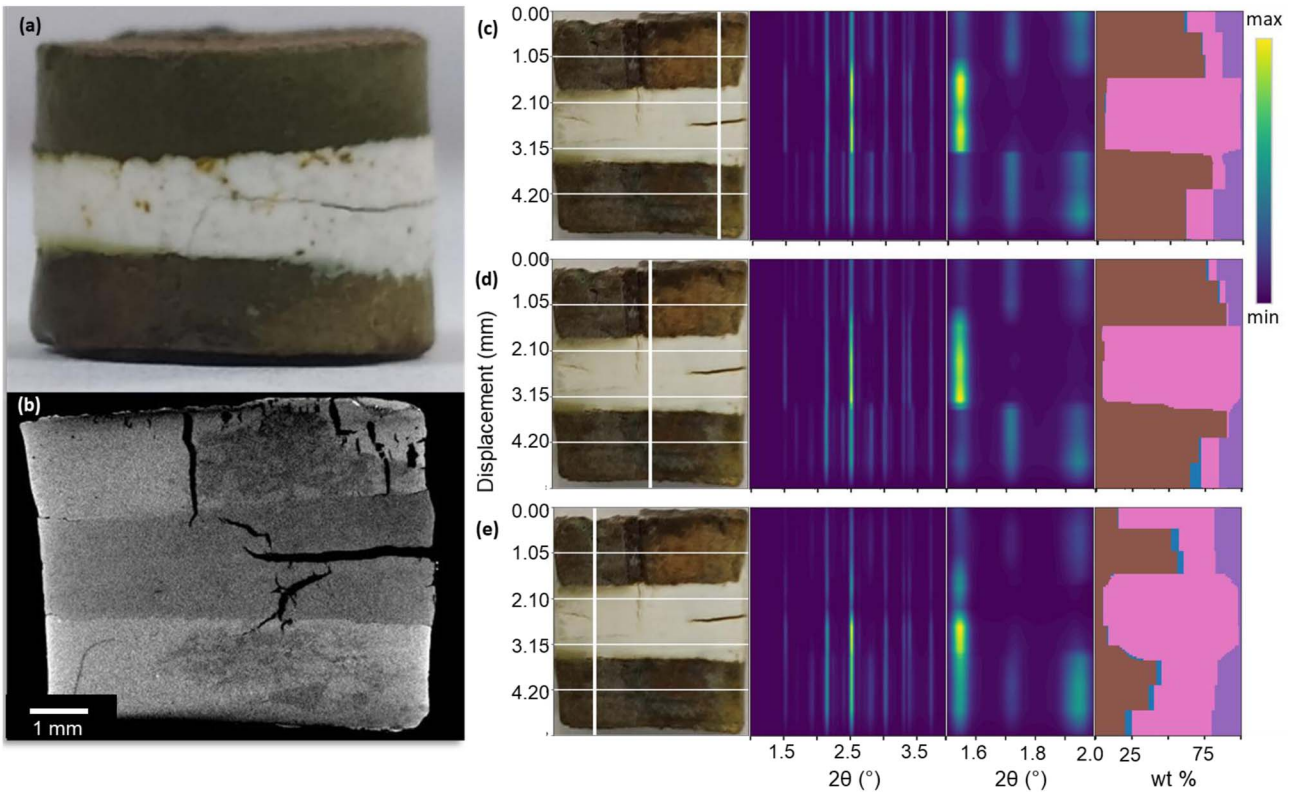

Fig. 10 Structural evolution across multilayered pellets. (a) Photograph of the sintered multilayer pellet. (b) X-ray tomography slice of the pellet, highlighting prominent cracking across the multilayer architecture. (c–e) Cross-sectional optical images (left), 1D X-ray diffraction heatmaps (center), and phase quantification *via* Rietveld refinement (right) for three sections of the sintered multilayer pellet: (c) least densified region, (d) intermediate region, and (e) most densified region. Major crystalline phases include LATP (pink), Al, Ti-doped LVP (brown), $Li_3V_2(PO_4)_3$ (blue), and oxidized ε-$LiVOPO_4$ (purple). Notably, the extent of LATP–LVP reaction increases in the less densified regions.

LVP–LATP|LATP interfaces may contribute to the widespread formation of ε-$LiVOPO_4$ across the multilayer, even in areas without clearly visible hotspots. Moreover, architectural limitations in thermal dissipation and current distribution—stemming from the multilayer's thicker, more complex structure—likely contribute to sustained local heating, supporting extended decomposition. The lack of clear spatial correlation between ε-$LiVOPO_4$ and hotspot location may also arise from the presence of multiple flash sites within the multilayer (as evidenced by several sites of localized shrinkage in Fig. 10e, S10c, and S11f and cracks along transversal and longitudinal directions), leading to a more diffuse and overlapping heat profile. Another contributing factor may be the competition for vanadium during phase evolution: the formation of Al, Ti-doped LVP draws vanadium from the LVP framework, potentially depleting precursors for ε-phase formation. This is supported by the observed inverse spatial correlation between the two impurity phases. Due to the extent of this reaction, unreacted LVP is largely absent in the multilayer, with <5 wt% remaining in most regions and completely undetectable in others (*e.g.*, in Fig. S10a).

In addition to the spatially resolved analysis, a densified section of the multilayer was ground and examined as a powder using higher-resolution diffraction. This enabled the identification of two minor secondary phases (~1 wt%) of $AlPO_4$ and $Li_4P_2O_7$. The corresponding Rietveld refinement and fitted values are presented in Fig. S12 and Table S8, respectively.

Despite extensive reactions within the composite layers, LVP–LATP|LATP interfaces did not exhibit distinct interfacial phases, nor measurable chemical gradients at the electrode–electrolyte boundaries, and mechanical contact across these interfaces was well preserved. This is supported by SEM and EDX analysis (Fig. 11), which reveal a sharp elemental transition between Ti-rich and V-rich regions with no visible interdiffusion, along with dense microstructures and low porosity in both LATP and composite layers. Although cracking occurred throughout the pellet, it did not preferentially propagate along the interfaces that maintain good interfacial cohesion, suggesting that EFS offers scope to improve mechanical integrity at the interface. Additional higher-magnification SEM images confirming the dense microstructure in both LATP and composite layers are provided in Fig. S13.

While the current EFS parameters achieved densification, the extent of decomposition within the composite layers and the migration of $V^{3+/4+}$ cations into the electrolyte indicate that alternative sintering conditions should be explored, including shorter or zero post-flash holds, thinner multilayers (more consistent with practical application needs), and optimized LATP : LVP ratios and particle size distributions should improve percolation pathways within the electrode layers, reducing current localization and thermal gradients. The introduction of percolating conductive pathways is also promising, as demonstrated in graphite-assisted flash sintering of Sm_2O_3-doped CeO_2,[79] where a conductive graphite network lowered flash onset and homogenized Joule heating. Even though carbon black was intentionally excluded in this study to isolate the intrinsic electrochemical sintering behavior of the LVP–LATP system, its eventual incorporation into full-stack configurations is feasible. While graphite and carbon black differ in crystallinity and electrical conductivity, a finely dispersed carbon black phase could provide comparable benefits—enhancing current homogeneity while mitigating electrode melting. However, altering the field distribution through carbon black additives may also introduce new decomposition pathways, such as localized reduction of Ti^{4+} in LATP, which should be carefully examined.

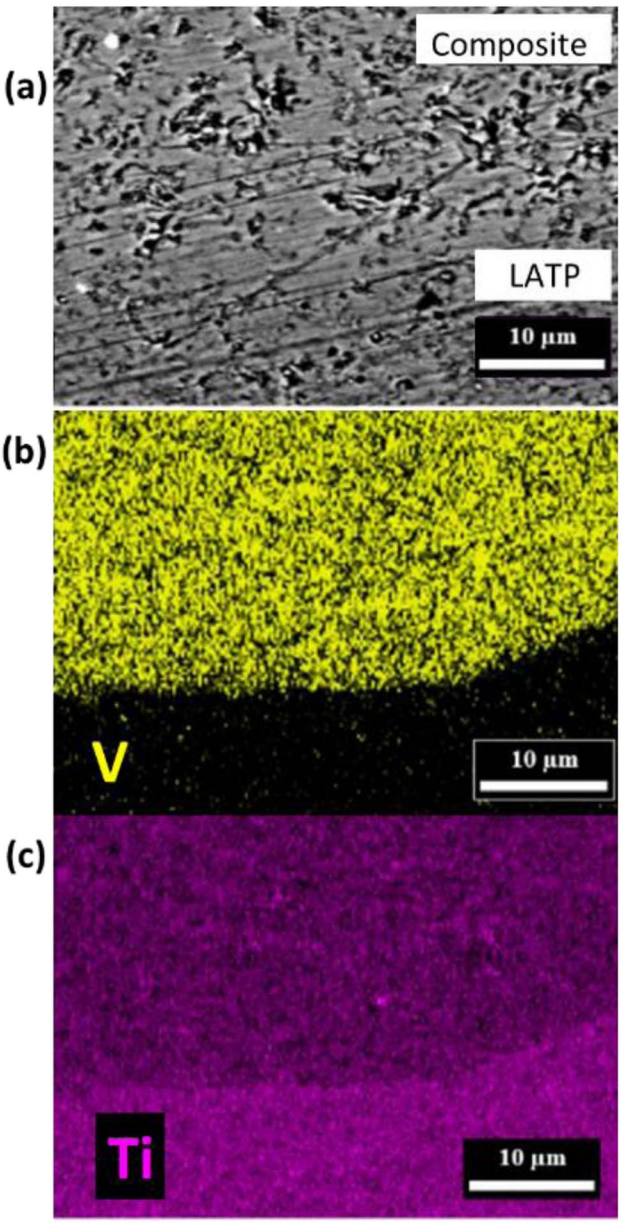

Fig. 11 Cross-sectional SEM and EDX analysis across the LATP|composite interface in the flash-sintered multilayer. (a) BSD image showing the interface between LATP and the composite layer. Longitudinal striations are artifacts from mechanical polishing during cross-section preparation. (b) EDX elemental map of vanadium, concentrated in the composite region. (c) EDX elemental map of titanium, predominantly located in the LATP layer.

Conclusion

We systematically evaluated how electric field parameters, particularly frequency, affect sintering outcomes across LATP, LVP, and their combinations. Single-phase LATP required high frequencies (≥100 kHz) to overcome its blocking behavior, but this also induced extreme local heating and electrode melting due to intense dielectric response. Conversely, LVP—being a mixed conductor—sintered effectively at lower frequencies (1–100 kHz), though partial phase decomposition occurred near hotspots.

Strikingly, LATP–LVP composite sintering was most effective at 1 kHz—a frequency previously insufficient for densifying either component alone. The composite exhibited dense microstructures, limited interdiffusion, and suppressed decomposition spatially confined within a smaller hotspot region, while conventional co-sintering of the same phases at 700 °C results in extensive reaction. These findings highlight how coupling pure ionic and mixed-conducting phases enables EFS by transforming electronic conductivity into Li^+ transport and Joule heating in otherwise resistive domains.

Building on this, we successfully EFS-processed a multilayer LVP–LATP|LATP|LVP–LATP monolith—demonstrating this approach can densify layered ASSLB architectures in a dry, single-step process. While compositional gradients and localized decomposition were still present, the interfaces remained mechanically coherent. Cracks did not preferentially propagate along the LATP–composite boundaries, and no enrichment of decomposition products was observed within the densified regions, confirming robust interfacial cohesion despite the overall chemical instability under the applied reaction parameters.

Altogether, this study establishes clear mechanistic distinctions between conventional and electrochemical flash sintering, revealing how electric-field distribution and redox activity dictate phase evolution and densification. By harnessing the electrochemical reactions during flash sintering, we demonstrate a pathway to exploit these reactions constructively for improving electrolyte–electrode interfacial connectivity in all-solid-state battery architectures through a dry, scalable process.

Future work will focus on thinner electrolytes, asymmetric cells, and the incorporation of conductive additives such as carbon black—an essential component in practical ASSLB cathodes—which could also promote field homogenization and stabilize flash onset during EFS. With growing mechanistic understanding and careful process optimization, EFS could offer a practical pathway toward scalable, single-step fabrication of next-generation solid-state batteries.

Experimental

Material synthesis

$Li_3V_2(PO_4)_3$ (LVP) was synthesized *via* solid-state reaction method following a procedure adapted from previous work.[68] Stoichiometric amounts of lithium carbonate (Li_2CO_3), vanadium oxide (V_2O_5), and ammonium dihydrogen phosphate ($NH_4H_2PO_4$) were thoroughly ground for 2 hours using a mortar and pestle. The homogeneous mixture was pre-calcined at 350 °C for 5 hours under a controlled atmosphere of Ar containing 10% H_2 to remove volatile gases. Subsequently, the mixture was re-ground for an additional 30 minutes before the final calcination step at 850 °C for 12 hours under the same atmosphere (Ar + 10% H_2).

$Li_{1.4}Al_{0.4}Ti_{1.6}(PO_4)_3$ (LATP) powder used in this study was commercially obtained from NEI Corporation (USA).

Sintering

LATP and LVP powders were planetary ball-milled in zirconia jars with isopropyl alcohol as the milling medium.[68,80] The processed powders were uniaxially pressed at 40 MPa, followed by cold isostatic pressing at 250 MP. The resulting pre-sintered pellets had an average relative density of about 65%.

Flash sintering was performed using a setup adapted from previous work[81,82] enabling concurrent impedance spectroscopy measurements and densification. The pellet-electrode assembly was placed inside a furnace with a controlled atmosphere. Two alternating current power supplies were used depending on the required frequency range: a Pacific 115-ASX generator for low- to mid-frequency experiments (15 Hz–1.2 kHz), and a custom-built power supply developed by Galtenco Solutions for higher-frequency operation (100 Hz–500 kHz). The output voltage and frequency were independently adjusted to match the flash sintering conditions. The applied electric field was adjusted to trigger flash based on impedance measurements, while the imposed current density governed the subsequent flash regime. Frequency and current density were varied to assess their influence on densification and phase evolution, whereas heating rate was not independently controlled due to the self-amplifying nature of the flash event. Post-flash hold time was also varied to evaluate its effect on phase stability. Conductive gold layers, platinum grids or felts, were placed between pellets and platinum electrodes to enhance current homogeneity and facilitate easy sample removal post-sintering.

For comparative studies, sintering conditions were adapted to the composition: single-phase LATP pellets were sintered at 1000 °C for 10 hours in air to achieve optimal densification and ionic conductivity,[80] while LATP–LVP composites (6 : 4 weight ratio) were sintered at 700, 750 and 800 °C for 3 hours under an Ar atmosphere to avoid phase decomposition and oxidation.[82]

Data acquisition

Powder samples were loaded into borosilicate capillary tubes with a diameter of 1 mm. The flash-sintered pellets were mounted onto Kapton tape. The multilayered pellet was cross-sectioned into three distinct regions (see SI Fig. S9). Background scattering from empty capillary tubes and Kapton tape was measured separately and subtracted from the sample data for accurate corrections.

Spatially resolved total scattering measurements were conducted at the XPDF I15-1 beamline at Diamond Light Source, UK. Samples were scanned along the *z*-direction under conditions of 76.69 keV energy ($\lambda = 0.161669$ Å) using a beam size of 700 μm (h) × 10 μm (v). Reducing the beam size in the vertical direction improved spatial resolution, enabling more accurate characterization of structural variations across the hotspot.

Data were recorded using a PerkinElmer XRD 4343 CT flat-panel detector, achieving a Q-range exceeding 25 $Å^{-1}$ at a detector distance of 350 mm.

Total scattering data were processed into PDFs using the Gudrun software.[83] The Q-range for PDF transformation was 0.5 $Å^{-1}$ to 24 $Å^{-1}$, employing a Top Hat function of 3 $Å^{-1}$ width and a minimum radius for Fourier transformation of 1 Å. A Lorch modification function with a width of 0.01 Å was applied to generate the PDF.

XRD experiments were carried out using a Bruker D8 Endeavour diffractometer, operating in Bragg–Brentano geometry. The X-ray source consisted of a copper anode emitting unfiltered Cu-Kα radiation.

Reciprocal-space data and PDFs were analysed using the NMF-mapping application available on pdfitc.org.[84] The active range was restricted from 1 to 20 Å for PDF and 1 to 15 $Å^{-1}$ for Reciprocal-space data. Iterative assessments were performed with 2–5 components.

Data analysis

Rietveld refinement of structural models against reciprocal-space data was carried out using TOPAS v7 Academic software.[85] The background was modeled using a Chebyshev polynomial function with 10 coefficients. The scale factor, zero-point correction, lattice parameters, atomic positions, occupancy factors, and isotropic atomic displacement parameters (Biso) were systematically refined. Si standard (NIST 640c) was used as the instrumental standard for the laboratory XRD and CeO_2 (NIST 674b) for total scattering measurement for accurate cell parameter determination. Preferred orientation effects were refined, where necessary, using the Spherical Harmonics function.

Author contributions

R. Fukada (RF) led the experimental investigation, data curation, formal analysis, validation, visualization, and writing – review & editing as part of his doctoral thesis work. M. Diaz-Lopez (MDL) conceived and funded the study (conceptualization, project administration, funding acquisition), co-supervised RF with C. V. Colin (CVC), and took the lead on methodology, visualization, writing – original draft, and writing – review & editing. CVC contributed to supervision and writing – review & editing. All three authors contributed to formal analysis, methodology development, validation, and visualization. T. Fabre (TF) is credited for resources and investigation, having supplied the pellets and associated microstructural data used in this study, both produced as part of his doctoral research. C. Marlu (CM) and R. Bouchet (RB), co-supervisors of TF's thesis, supported the project through early material development and manuscript review.

Conflicts of interest

The authors declare that they have no known competing financial interests or personal relationships that could have appeared to influence the work reported in this paper.

Data availability

The data used to support the conclusions of this study are available from the corresponding author upon reasonable request. The data supporting this article have been included as part of the supplementary information (SI). Supplementary information is available. See DOI: https://doi.org/10.1039/d6ta00082g.

Acknowledgements

The authors acknowledge Diamond Light Source for time on beamline I15-1 under proposal CY30870. The pellets used in this study were synthesized during the ANR-20-CE05-0040-02 project as part of TF's thesis. The experimental analysis and interpretation were carried out as part of RF's doctoral thesis, within the framework of the Chaire de Professeur Junior (CPJ) MatInnov program, which also supports the CPJ position held by MDL.

References

1 J. Janek and W. G. Zeier, *Nat. Energy*, 2016, **1**(9), 1.
2 Y. Tian, G. Zeng, A. Rutt, T. Shi, H. Kim, J. Wang, J. Koettgen, Y. Sun, B. Ouyang, T. Chen, Z. Lun, Z. Rong, K. Persson and G. Ceder, *Chem. Rev.*, 2021, **121**, 1623.
3 J. W. Fergus, *J. Power Sources*, 2010, **195**, 4554.
4 P. Knauth, *Solid State Ionics*, 2009, **180**, 911.
5 P. Albertus, V. Anandan, C. Ban, N. Balsara, I. Belharouak, J. Buettner-Garrett, Z. Chen, C. Daniel, M. Doeff, N. J. Dudney, B. Dunn, S. J. Harris, S. Herle, E. Herbert, S. Kalnaus, J. A. Libera, D. Lu, S. Martin, B. D. McCloskey, M. T. McDowell, Y. S. Meng, J. Nanda, J. Sakamoto, E. C. Self, S. Tepavcevic, E. Wachsman, C. Wang, A. S. Westover, J. Xiao, *et al.*, *ACS Energy Lett.*, 2021, **6**, 1399.
6 J. Li, C. Ma, M. Chi, C. Liang, N. J. Dudney, J. Li, N. J. Dudney, C. Ma, M. Chi and C. Liang, *Adv. Energy Mater.*, 2015, **5**, 1401408.
7 X. Han, Y. Gong, K. Fu, X. He, G. T. Hitz, J. Dai, A. Pearse, B. Liu, H. Wang, G. Rubloff, Y. Mo, V. Thangadurai, E. D. Wachsman and L. Hu, *Nat. Mater.*, 2017, **16**(5), 572.
8 D. J. Lee, Y. Jeon, J. P. Lee, L. Zhang, K. H. Koh, F. Li, A. U. Mu, J. Wu, Y. T. Chen, S. McNulty, W. Tang, M. Vicencio, D. Xu, J. Kim and Z. Chen, *Nat. Commun.*, 2025, **16**(1), 1.
9 H. Su, P. Li, N. Mao, R. Li, X. Zhao, Y. Li, W. Zhou, and X. Zhou, *Green Energy and Intelligent Transportation*, 2025, 100336.
10 M. Dixit, C. Beamer, R. Amin, J. Shipley, R. Eklund, N. Muralidharan, L. Lindqvist, A. Fritz, R. Essehli, M. Balasubramanian and I. Belharouak, *ACS Energy Lett.*, 2022, **7**, 3936.
11 A. C. Luntz, J. Voss and K. Reuter, *J. Phys. Chem. Lett.*, 2015, **6**, 4599.
12 Y. Ren, T. Danner, A. Moy, M. Finsterbusch, T. Hamann, J. Dippell, T. Fuchs, M. Müller, R. Hoft, A. Weber, L. A. Curtiss, P. Zapol, M. Klenk, A. T. Ngo, P. Barai,

B. C. Wood, R. Shi, L. F. Wan, T. W. Heo, M. Engels, J. Nanda, F. H. Richter, A. Latz, V. Srinivasan, J. Janek, J. Sakamoto, E. D. Wachsman and D. Fattakhova-Rohlfing, *Adv. Energy Mater.*, 2023, **13**, 202201939.
13 M. Balaish, K. J. Kim, H. Chu, Y. Zhu, J. C. Gonzalez-Rosillo, L. Kong, H. Paik, S. Weinmann, Z. D. Hood, J. Hinricher, L. J. Miara and J. L. M. Rupp, *Chem. Soc. Rev.*, 2025, **54**, 8925.
14 A. Sazvar, M. Hajibandeh, P. Vafaei, E. Hosseinzadeh and M. Jabbari, *J. Energy Storage*, 2024, **101**, 113863.
15 H. Shen, Z. Jia, Y. Zhang, S. Chen, Z. Huang, F. Shangguan, S. Yan, T. Zhang, K. Chen, W. Xue, Y. Wu, W. Tang and Y. L. He, *Adv. Mater.*, 2025, e15467.
16 J. Minkiewicz, G. M. Jones, S. Ghanizadeh, S. Bostanchi, T. J. Wasely, S. A. Yamini and V. Nekouie, *Open Ceram.*, 2023, **16**, 100497.
17 G. Delaizir, V. Viallet, A. Aboulaich, R. Bouchet, L. Tortet, V. Seznec, M. Morcrette, J. M. Tarascon, P. Rozier and M. Dollé, *Adv. Funct. Mater.*, 2012, **22**, 2140.
18 R. Chaim, G. Chevallier, A. Weibel and C. Estournès, *J. Mater. Sci.*, 2017, **53**(5), 3087.
19 H. Yamada, T. Ito and R. Hongahally Basappa, *Electrochim. Acta*, 2016, **222**, 648.
20 S. W. Baek, J. M. Lee, T. Y. Kim, M. S. Song and Y. Park, *J. Power Sources*, 2014, **249**, 197.
21 J. Xue, K. Zhang, D. Chen, J. Zeng and B. Luo, *Mater. Res. Express*, 2020, **7**, 025518.
22 M. Kotobuki and M. Koishi, *J. Alloys Compd.*, 2020, **826**, 154213.
23 K. Waetzig, A. Rost, C. Heubner, M. Coeler, K. Nikolowski, M. Wolter and J. Schilm, *J. Alloys Compd.*, 2020, **818**, 153237.
24 G. Courbaron, R. B. Nuernberg, J. S. Sevillano, U. C. Chung, M. Duttine, C. Labrugère-Sarroste, J. Olchowka, D. Carlier, N. Delpuech and L. Croguennec, *J. Alloys Compd.*, 2024, **985**, 174062.
25 C. M. Chang, Y. Lee, S. H. Hong and H. M. Park, *J. Am. Ceram. Soc.*, 2005, **88**, 1803.
26 T. Tezuka, Y. Inagaki, S. Kodama, H. Takeda and I. Yanase, *Powder Technol.*, 2023, **429**, 118870.
27 P. H. Lai, B. J. Jacob, R. H. Colby, E. D. Gomez and B. D. Vogt, *Materialia*, 2024, **38**, 102238.
28 S. S. Berbano, J. Guo, H. Guo, M. T. Lanagan and C. A. Randall, *J. Am. Ceram. Soc.*, 2017, **100**, 2123.
29 J. H. Seo, Z. Fan, H. Nakaya, R. Rajagopalan, E. D. Gomez, M. Iwasaki and C. A. Randall, *Jpn. J. Appl. Phys.*, 2021, **60**, 037001.
30 X. Wang, J. Wang, F. Li, F. Zhu and C. Ma, *Ceram. Int.*, 2020, **46**, 18544.
31 H. Kim, S. Choi, D. H. Peck and S. Y. Yoon, *Ceram. Int.*, 2023, **49**, 8718.
32 T. Fabre, F. Fournet-Fayard, M. C. Steil and R. Bouchet, *Electrochim. Acta*, 2026, **552**, 148192.
33 R. I. Todd, E. Zapata-Solvas, R. S. Bonilla, T. Sneddon and P. R. Wilshaw, *J. Eur. Ceram. Soc.*, 2015, **35**, 1865.
34 M. Cologna, B. Rashkova and R. Raj, *J. Am. Ceram. Soc.*, 2010, **93**, 3556.
35 M. Biesuz and V. M. Sglavo, *J. Eur. Ceram. Soc.*, 2019, **39**, 115.
36 R. Raj, *J. Eur. Ceram. Soc.*, 2012, **32**, 2293.
37 C. E. J. Dancer, *Mater. Res. Express*, 2016, **3**, 102001.
38 M. Yu, S. Grasso, R. Mckinnon, T. Saunders and M. J. Reece, *Adv. Appl. Ceram.*, 2017, **116**, 24.
39 K. S. N. Vikrant, H. Wang, A. Jana, H. Wang and R. E. García, *npj Comput. Mater.*, 2020, **6**(1), 1.
40 R. Chaim, G. Chevallier, A. Weibel and C. Estournès, *J. Appl. Phys.*, 2017, **121**, 145103.
41 T. Yamamoto, *Mater. Trans.*, 2023, **64**, 2059.
42 G. M. Jones, M. Biesuz, W. Ji, S. F. John, C. Grimley, C. Manière and C. E. J. Dancer, *MRS Bull.*, 2021, **46**, 59.
43 J. P. Gittings, C. R. Bowen, A. C. E. Dent, I. G. Turner, F. R. Baxter and J. B. Chaudhuri, *Acta Biomater.*, 2009, **5**, 743.
44 J. S. C. Francis, M. Cologna, D. Montinaro and R. Raj, *J. Am. Ceram. Soc.*, 2013, **96**, 1352.
45 R. Muccillo, D. Z. de Florio, F. C. Fonseca, S. G. M. Carvalho and E. N. S. Muccillo, *Int. J. Appl. Ceram. Technol.*, 2022, **19**, 906.
46 J. V. Campos, I. R. Lavagnini, J. G. Pereira da Silva, J. A. Ferreira, R. V. Sousa, R. Mücke, O. Guillon and E. M. J. A. Pallone, *Scr. Mater.*, 2020, **186**, 1.
47 M. Lachal, H. El Khal, D. Bouvard, J. M. Chaix, R. Bouchet and M. C. Steil, *J. Am. Ceram. Soc.*, 2021, **104**, 3845.
48 Y. Xiao, Y. Wang, S. H. Bo, J. C. Kim, L. J. Miara and G. Ceder, *Nat. Rev. Mater.*, 2019, **5**(2), 105.
49 S. Yu, S. Schmohl, Z. Liu, M. Hoffmeyer, N. Schön, F. Hausen, H. Tempel, H. Kungl, H. D. Wiemhöfer and R. A. Eichel, *J. Mater. Chem. A*, 2019, **7**, 3882.
50 S. Yu, A. Mertens, H. Tempel, R. Schierholz, H. Kungl and R. A. Eichel, *ACS Appl. Mater. Interfaces*, 2018, **10**, 22264.
51 S. C. Yin, H. Grondey, P. Strobel, M. Anne and L. F. Nazar, *J. Am. Chem. Soc.*, 2003, **125**, 10402.
52 K. Arbi, M. Hoelzel, A. Kuhn, F. García-Alvarado and J. Sanz, *Inorg. Chem.*, 2013, **52**, 9290.
53 H. Aono, E. Sugimoto, Y. Sadaoka, N. Imanaka and G. Adachi, *J. Electrochem. Soc.*, 1990, **137**, 1023.
54 F. Ichihara, K. Niitsu, Y. Tanaka, Y. Niwa, K. Mitsuishi, S. Miyoshi, T. Ohno and T. Masuda, *J. Phys. Chem. C*, 2023, **127**, 15043.
55 J. P. Beaupain, K. Waetzig, H. Auer, N. Zapp, K. Nikolowski, M. Partsch, M. Kusnezoff and A. Michaelis, *Batteries*, 2023, **9**, 543.
56 F. Ichihara, S. Miyoshi and T. Masuda, *Phys. Chem. Chem. Phys.*, 2022, **24**, 25878.
57 K. Nagata and T. Nanno, *J. Power Sources*, 2007, **174**, 832.
58 Y. Liu, J. Chen and J. Gao, *Solid State Ionics*, 2018, **318**, 27.
59 B. Aman, S. Acharya and B. Reeja-Jayan, *Adv. Eng. Mater.*, 2024, **26**, 2302065.
60 O. Guillon, J. Gonzalez-Julian, B. Dargatz, T. Kessel, G. Schierning, J. Räthel and M. Herrmann, *Adv. Eng. Mater.*, 2014, **16**, 830.
61 L. Karacasulu, C. Manière, C. Vakifahmetoglu, S. Marinel and M. Biesuz, *Annu. Rev. Mater. Res.*, 2025, **55**, 203.
62 L. Porz, M. Scherer, D. Huhn, L. M. Heine, S. Britten, L. Rebohle, M. Neubert, M. Brown, P. Lascelles, R. Kitson, D. Rettenwander, L. Fulanovic, E. Bruder, P. Breckner, D. Isaia, T. Frömling, J. Rödel and W. Rheinheimer, *Mater. Horiz.*, 2022, **9**, 1717.

63 O. Guillon, W. Rheinheimer and M. Bram, *Adv. Eng. Mater.*, 2023, **25**, 2201870.
64 J. M. Chaix, R. Bouchet, D. Bouvard, T. Fabre, T. Garnault, C. Harnois, K. Koutoati, M. Lachal, S. Marinel and M. C. Steil, *Adv. Eng. Mater.*, 2023, **25**, 2201742.
65 R. DeWees and H. Wang, *ChemSusChem*, 2019, **12**, 3713.
66 J. V. Campos, I. R. Lavagnini, V. M. Zallocco, L. M. Jesus and A. C. M. Rodrigues, *J. Am. Ceram. Soc.*, 2024, **107**, 1806.
67 Z. Thatcher, C. H. Liu, L. Yang, B. C. McBride, G. T. Tran, A. Wustrow, M. A. Karlsen, J. R. Neilson, D. B. Ravnsbæk and S. J. L. Billinge, *Acta Crystallogr.*, 2022, **A78**, 242.
68 T. Fabre, M. Lachal, H. Raj, V. Pralong, R. Bouchet and M. C. Steil, *J. Eur. Ceram. Soc.*, 2025, **45**, 116941.
69 H. Zhang, H. Zhou, Z. Deng, L. Luo, S. P. Ong, C. Wang, H. Xin, M. S. Whittingham and G. Zhou, *ACS Appl. Mater. Interfaces*, 2023, **15**, 963.
70 N. Membreño, P. Xiao, K. S. Park, J. B. Goodenough, G. Henkelman and K. J. Stevenson, *J. Phys. Chem. C*, 2013, **117**, 11994.
71 R. Zhang, S. Yang, H. Li, T. Zhai, H. Li, *Air Sensitivity of Electrode Materials in Li/Na Ion Batteries: Issues and Strategies*, Vol. 4, John Wiley and Sons Inc, 2022.
72 S. C. Yin, P. S. Strobel, H. Grondey and L. F. Nazar, *Chem. Mater.*, 2004, **16**, 1456.
73 M. Sato, H. Ohkawa, K. Yoshida, M. Saito, K. Uematsu and K. Toda, *Solid State Ionics*, 2000, **135**, 137.
74 D. O. Semykina, O. A. Podgornova, S. B. Moodakare, R. Vedarajan and N. V. Kosova, *Inorg. Chem.*, 2023, **62**, 5939.
75 H. Feng, L. Guan, M. Li, Q. Fan, Y. Huang, X. Song and S. An, *J. Eur. Ceram. Soc.*, 2024, **44**, 4731.
76 S. Molina-Molina, A. Perejón, L. A. Pérez-Maqueda and P. E. Sánchez-Jiménez, *Ceram. Int.*, 2023, **49**, 14834.
77 M. Gellert, E. Dashjav, D. Grüner, Q. Ma and F. Tietz, *Ionics*, 2018, **24**, 1001.
78 M. Malaki, J. Haust, J. P. Beaupain, H. Auer, A. Beyer, K. Wätzig, M. Kusnezoff and K. Volz, *Adv. Mater. Interfaces*, 2023, **10**, 2300513.
79 L. Guan, J. Li, X. Song, J. Bao and T. Jiang, *Scr. Mater.*, 2019, **159**, 72.
80 H. Raj, T. Fabre, M. Lachal, A. Neveu, J. Jean, M. C. Steil, R. Bouchet and V. Pralong, *ACS Appl. Energy Mater.*, 2023, **6**, 1197.
81 M. C. Steil, D. Marinha, Y. Aman, J. R. C. Gomes and M. Kleitz, *J. Eur. Ceram. Soc.*, 2013, **33**, 2093.
82 T. Fabre, *Frittage flash de céramiques conductrices ioniques et mixtes (électronique-ioniques) pour application dans les batteries tout solide*, 2024.
83 A. K. Soper and E. R. Barney, *J. Appl. Crystallogr.*, 2011, **44**, 714.
84 L. Yang, E. A. Culbertson, N. K. Thomas, H. T. Vuong, E. T. S. Kjær, K. M. Ø. Jensen, M. G. Tucker and S. J. L. Billinge, *Acta Crystallogr.*, 2021, **A77**, 2–6.
85 A. A. Coelho, *J. Appl. Crystallogr.*, 2018, **51**, 210–218.